Article

Carbon-Conjugated Co Complexes as Model Electrocatalysts for Oxygen Reduction Reaction

Qidi Sun [1,2], Qing Wang [1], Fuzhi Li [1], Yizhe Liu [2], Xintong Li [2], Zonglong Zhu [2], Jianlin Chen [3], Yung-Kang Peng [2,*] and Jun Gu [1,*]

[1] Department of Chemistry, Southern University of Science and Technology, Shenzhen 518055, China
[2] Department of Chemistry, City University of Hong Kong, Kowloon 999077, Hong Kong
[3] Department of Applied Science, School of Science and Technology, Hong Kong Metropolitan University, Good Shepherd Street, Ho Man Tin, Kowloon 999077, Hong Kong
[*] Correspondence: ykpeng@cityu.edu.hk (Y.-K.P.); guj6@sustech.edu.cn (J.G.)

Abstract: Single-atom catalysts are a family of heterogeneous electrocatalysts widely used in energy storage and conversion. The determination of the local structure of the active metal sites is challenging, which limits the establishment of the reliable structure-property relationship of single-atom catalysts. A carbon black-conjugated complex can be used as the model catalyst to probe the intrinsic activity of metal sites with certain local structures. In this work, we prepared carbon black-conjugated [Co(phenanthroline)Cl$_2$], [Co(o-phenylenediamine)Cl$_2$] and [Co(salophen)]. In these catalysts, the Co complexes with well-defined structures are anchored on the edge of carbon black by pyrazine moieties. The number of electrochemical accessible Co sites can be measured from the area of the redox peaks of pyrazine linkers in the cyclic voltammetry curve. Then, the intrinsic electrocatalytic activity of one Co site can be obtained. The catalytic performances of the three catalysts towards oxygen reduction reaction in alkaline conditions were measured. Carbon black-conjugated [Co(salophen)] showed the highest intrinsic activity with the turnover frequency of 0.72 s^{-1} at 0.75 V vs. the reversible hydrogen electrode. The strategy developed in this work can be used to explore and verify the possible local structure of active sites proposed for single-atom catalysts.

Keywords: electrocatalysis; single-atom catalyst; model catalyst; oxygen reduction reaction; Co complex

1. Introduction

Transition metal-nitrogen-carbon (TM-N-C) single-atom catalysts have received extensive research interest in recent years since these types of catalysts are composed of only earth-abundant elements and exhibit outstanding electrocatalytic activity towards small-molecule activation processes such as oxygen reduction reaction (ORR) and CO$_2$ reduction reaction [1–5]. The most widely used method to prepare this type of material is the pyrolysis of metal-containing organic precursors, such as metal-organic frameworks (MOFs) [6–10]. The most proposed structure of the active site is the TM-N$_x$ center (transition metal atom coordinated with N ligands) embedded in an N-doped graphitic-type carbon matrix [11–13]. The TM site coordinated with C, O and S ligands is also regarded as the active site in some reports [14–16], and the TM site with a low coordination number at the edge of the carbon matrix is considered more active in some reports [17–19]. However, precise control of the atomic-level structure of catalysts is extremely difficult in the pyrolysis method. TM sites with different local structures, namely TM atoms with different coordination numbers, coordinated with different elements or the same element with different types (such as pyridinic N and pyrrolic N), may coexist in the pyrolyzed product [20–22]. Moreover, the local structure of TM sites is difficult to characterize due to the un-uniqueness of the local structure and the amorphous nature of the material. At the

moment, the determination of the coordination number, coordinated element and the type of ligands heavily depend on the fitting of extended X-ray absorption fine structure (EXAFS) and X-ray photoelectron spectroscopy (XPS), which typically have high uncertainty [23–26]. To investigate the structure–property relationship, model catalysts with well-defined local structures of TM sites are highly demanded.

TM-N-C single-atom catalysts can be regarded as complexes with solid-state ligands. Investigation into the well-defined TM complex grafted onto carbon black (CB) may help to understand the structure-property relationship. The TM single-atom catalysts fabricated via the pyrolysis of precursors are usually characterized by metal sites embedded in the hexagonal structure of the carbon substrate. Therefore, CB-anchored TM complexes with phenyl-type ligands can possibly mimic TM-N-C single-atom catalysts prepared using pyrolysis methods. Surendranath et al. developed a conjugating method by using an aromatic pyrazine motif to link the complex to the edge of graphitic carbon support [27–33]. Similar to the TM sites in TM-N-C single-atom catalysts, TM sites in this conjugated complex are in the same plane with the graphitic carbon layer, and the orbitals of TM are coupled to the delocalized π-system of the carbon support [29]. Therefore, this method provides an excellent platform to investigate the reliable relationship between the local coordination structure of TM sites and their catalytic properties.

In this work, we prepared three CB-conjugated Co complexes, namely, [Co (phenanthroline)Cl$_2$] (CB-phen-Co), [Co(o-phenylenediamine)Cl$_2$] (CB-pda-Co) and [Co (salophen)] (CB-salophen-Co) by anchoring the corresponding complex onto the CB by pyrazine linker, as illustrated in Scheme 1. These complexes were used as model heterogeneous electrocatalysts for ORR under alkaline conditions. The number of electrochemically accessible Co sites can be measured from the area of the redox peaks of the pyrazine linkers in cyclic voltammetry (CV) curves. Thus, the turnover frequencies (TOFs) of the TM sites were measured. The TOF of ORR increased in the order of CB-phen-Co < CB-pda-Co < CB-salophen-Co.
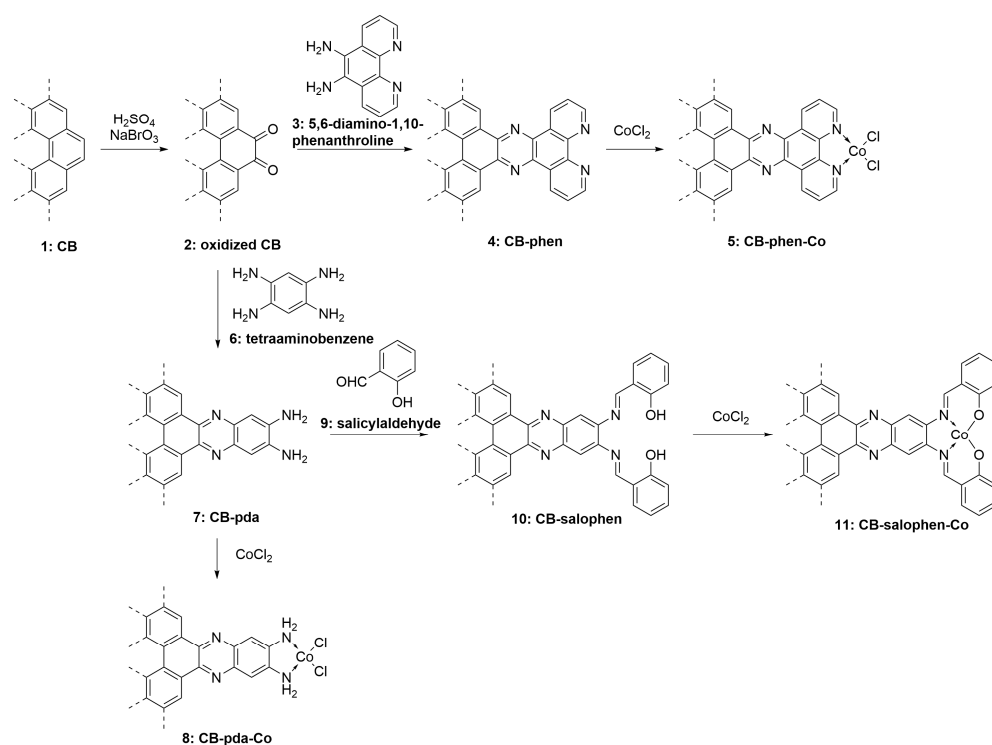
Scheme 1. Strategy to prepare CB-conjugated Co complexes.

2. Results and Discussion

2.1. Morphology and Structural Characterization

XRD and aberration-corrected TEM were used to characterize the existing form of Co in the three CB-conjugated complexes. In the XRD patterns (Figure 1a), the broad diffraction peaks at 26° and 42° correspond to the (002) and (101) diffractions of hexagonal graphite generated by the CB, which are similar to those of carbon-conjugated ligands without TMs (Figure S1). No diffraction peaks of Co-containing species are observed. Figure 1b–d show the HAADF-STEM images of the CB-conjugated complexes. The bright spots highlighted by the red circles show the discrete Co sites. The CB we used (Ketjen black) is not a flat single-layer material, such as graphene. Instead, it is porous and contains multiple carbon layers. Therefore, the thick regions with a high density of bright spots in the HAADF-STEM images may be the projection of the multi-layer parts of the materials. Moreover, when $CoCl_2$ was dissolved in anhydrous ethanol and stirred for 1 day under an Ar atmosphere at ambient temperature, no solid-state products were formed. These results indicate that Co-containing particles, such as oxide or hydroxide, were not formed, and isolated Co sites were loaded on the CB.
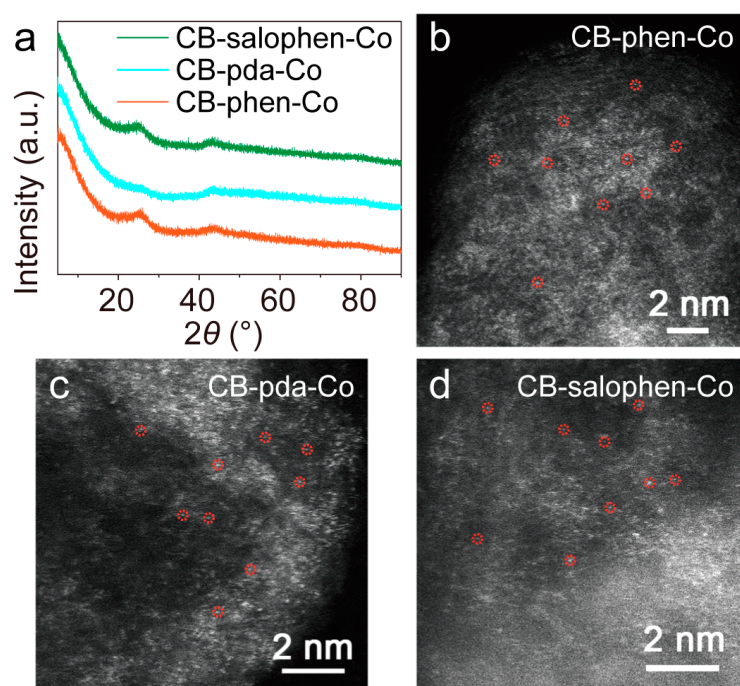

Figure 1. Characterization of CB-conjugated complexes. (**a**) XRD patterns. HAADF-STEM images of (**b**) CB-phen-Co, (**c**) CB-pda-Co, and (**d**) CB-salophen-Co.

XPS was used to monitor the oxidation of CB, the conjugation of the ligands and the chelation of Co^{2+} cations. Figure 2 shows the XPS survey spectra. After CB was oxidized, the intensity of O 1s peaked around 530 eV and the O KLL Auger signal around 970 eV increased drastically (curve 2). After the conjugation of the ligands on the oxidized CB, N1s peaks around 400 eV appeared (curves 4, 7, 10). Figure S2 compares the O 1s spectra of oxidized CB before and after the reaction with *o*-phenylenediamine. Each spectrum was deconvoluted into a peak of the hydroxy group (533.4 eV) and a peak of the carbonyl group (531.7 eV) [34]. After the reaction, the relative intensity of the peak of the carbonyl group decreased considerably, confirming that *o*-quinone moieties on the oxidized CB can react with diamine moieties to form pyrazine structures. Furthermore, after the addition of Co^{2+} cations to the CB-conjugated ligands, Co 2p peaks around 780 eV were observed (curves 5, 11, 8 in Figure 2). Cl 2p peaks around 200 eV were observed in the XPS spectra of CB-phen-Co (curve 5) and CB-pda-Co (curve 8), while not observed in that of CB-salophen-Co (curve 11), which is consistent with their proposed structures shown in Scheme 1.
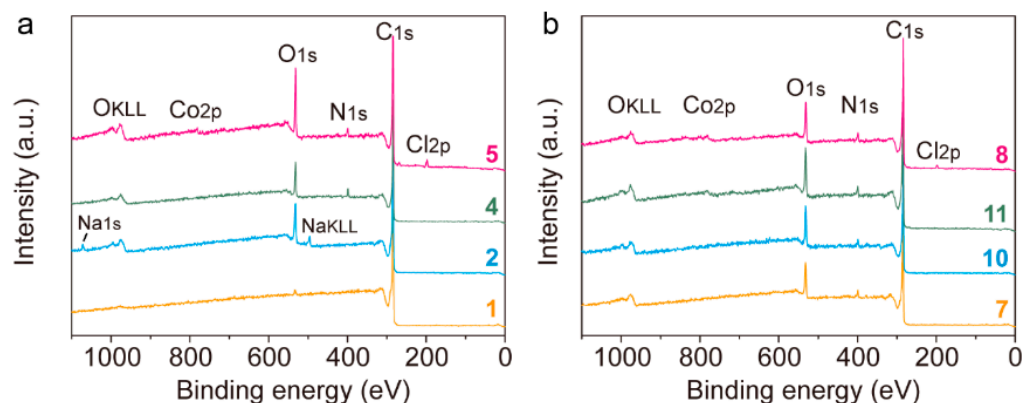
Figure 2. Survey XPS spectra of (**a**) CB (1), oxidized CB (2), CB-phen (4), CB-phen-Co (5) and (**b**) CB-pda (7), CB-salophen (10), CB-salophen-Co (11) and CB-pda-Co. The number of each spectrum refers to the sample with the structure shown in Scheme 1.

Table 1 lists the atomic composition of the three CB-conjugated Co complexes detected by XPS. The ideal N:Co atomic ratio of the three complexes should be four, according to their proposed structures. Considering that the element content determined by XPS typically shows an error of approximately 20%, the experimental N:Co atomic ratios in Table 1 are reasonably around the ideal ratio [35]. The ideal Cl:Co atomic ratio of CB-phen-Co and CB-pda-Co should be two. The experimental value of CB-phen-Co was slightly lower than two, while that of CB-pda-Co was substantially lower than two. We ascribed these discrepancies to the fact that the Cl$^-$ ligands were partially substituted by OH$^-$ or H$_2$O, and the Co-Cl coordination in [Co(pda)Cl$_2$] is weaker than that in [Co(phen)Cl$_2$]. Although Cl$^-$ ligands were involved in the pristine CB-pda-Co and CB-phen-Co, during the ORR process in KOH electrolyte, all of the Cl$^-$ ligands were substituted by OH$^-$, as indicated by the XPS surveys of CB-pda-Co and CB-phen-Co after electrocatalytic measurements (Figure S3). It is noteworthy that the weight fractions of Co in the CB-conjugated complexes deduced from XPS analysis were higher than that from ICP-MS (Table S1), indicating that the surface part of CB grafted more complexes than the inner part of the CB.

Table 1. Atomic composition (in percentage) of CB conjugated Co complexes detected by XPS.

	C	O	N	Co	Cl	N:Co	Cl:Co
CB-phen-Co	79.03%	16.65%	2.50%	0.64%	1.17%	3.91	1.83
CB-pda-Co	81.18%	13.12%	4.22%	1.01%	0.46%	4.18	0.46
CB-salophen-Co	81.75%	13.60%	3.75%	0.90%	N/A	4.17	N/A

The coordination between N ligands and Co^{2+} cations was characterized by using N 1s XPS. Figure 3 shows the spectra of CB-phen and CB-phen-Co. In the spectrum of CB-phen (Figure 3a), the peak at 399.3 eV was assigned to pyrazine and phenanthroline moieties [36]. The spectrum of CB-phen-Co was deconvoluted into a peak at 399.3 eV and a peak at 400.3 eV, corresponding to pyrazine moieties and pyridinic N coordinated with Co^{2+} cations [37,38]. The two peaks possessed similar areas. Since the electron donation from pyridinic N to Co^{2+} cations led to decreased electron density on N atoms, the N 1s binding energy of the N atoms coordinated with Co^{2+} was higher than that of the N atoms in the pyrazine moieties.
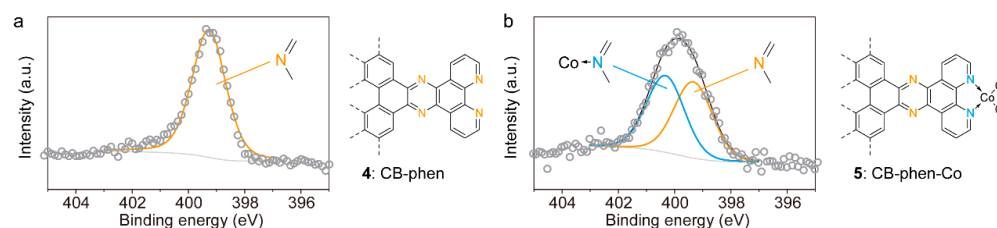
Figure 3. N 1s XPS of (**a**) CB-phen and (**b**) CB-phen-Co. Circles show the data and lines show the fitting curves.

Figure 4a,b compare the N 1s spectra of CB-pda and CB-pda-Co. Both spectra were deconvoluted into a peak at 399.3 eV and a peak at 400.4 eV with similar areas. The peaks at 399.3 eV in both spectra were assigned to pyrazine moieties. For CB-pda, the peak at 400.4 eV was assigned to the amino group (Figure 4a) [39], while for CB-pda-Co, this peak was assigned to the amino group coordinated with Co^{2+} (Figure 4b) [40]. The N 1s spectra of [Co(pda)Cl$_2$] complex shows the peak at 400.4 eV (Figure 4c), indicating that the formation of a coordination bond with Co^{2+} did not lead to a significant change in the binding energy of the N atom in the amino group.
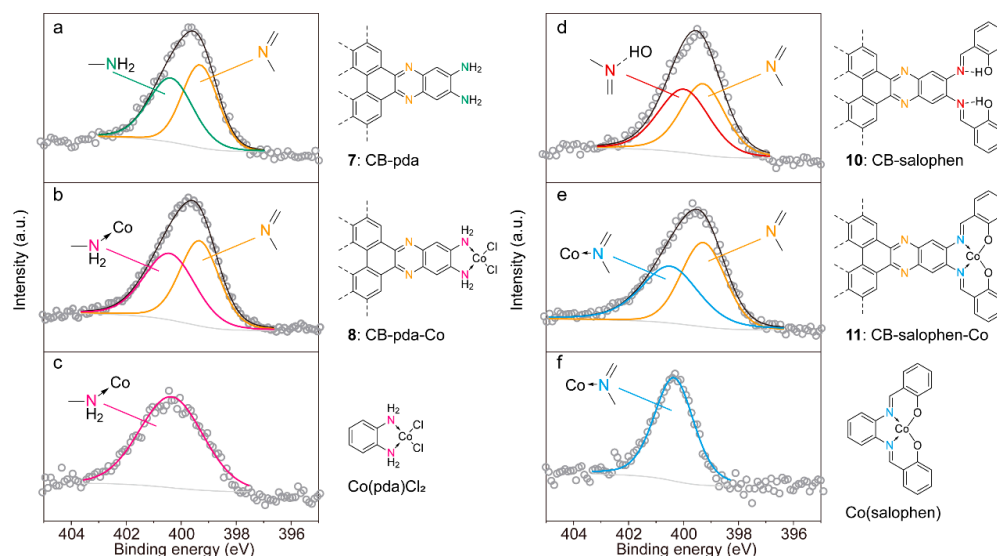

Figure 4. N 1s XPS of (**a**) CB-pda, (**b**) CB-pda-Co, (**c**) [Co(pda)Cl$_2$], (**d**) CB-salophen, (**e**) CB-salophen-Co and (**f**) Co(salophen). Circles show the data and lines show the fitting curve.

Figure 4d,e compare the N 1s spectra of CB-salophen and CB-salophen-Co. The spectrum of CB-salophen was deconvoluted into a peak at 399.3 eV, assigned to pyrazine moieties, and a peak at 400.0 eV, assigned to the imine moieties (Figure 4d). Since the intramolecular hydrogen bond between the phenolic hydroxy group and imine N in CB-salophen lowered the electron density of N, the binding energy of this kind of imine N was considerably higher than that of pyrazine moieties [41]. The spectrum of CB-salophen-Co was deconvoluted into a peak at 399.3 eV, also assigned to pyrazine moieties, and a peak at 400.4 eV, assigned to imine N coordinated with Co^{2+} (Figure 4e). The areas of the two peaks are similar. This assignment is supported by the spectrum of Co(salophen), which shows a single peak at 400.4 eV (Figure 4f).

Infrared (IR) spectra were further used to confirm that the complexes with the proposed structures were anchored on CB. As shown in Scheme S1, small-molecule analogs of the CB-conjugated complexes were prepared with a similar method, except that oxidized CB in Scheme 1 was replaced by 9,10-phenanthrenequinone (PAQ). As shown in Figure S4, the difference spectra of CB-conjugated complexes and oxidized CB (CB-complex–oxidized CB) are similar to the spectra of the corresponding PAQ-conjugated complexes. More

importantly, the stretching of C=N bonds [42] in the pyrazine moieties at 1635 cm^{-1} was observed in all the spectra. These results confirm that the complexes with the proposed structures were successively anchored on CB by pyrazine moieties.

2.2. Electrochemical Measurements

One major advantage of CB-conjugated complexes as model electrocatalysts is that the mole of electrochemical accessible catalytic sites can be measured by the electrochemical method. Then, it is possible to calculate the intrinsic TOF of one catalytic site. In general, when a powder sample is deposited on a conducting substrate such as glassy carbon, not all of the catalytic sites are exposed to the electrolyte solution and accessible to the reaction substrate. Therefore, if we consider all the metal atoms in a single-atom catalyst as catalytic sites that contribute equivalently to the overall activity, we will underestimate the value of TOF. Thanks to the reversible redox process of pyrazine moieties in CB-conjugated complexes [28], the mole of electrochemical active catalytic sites is measurable. Figure 5a shows the CV curve of phenazine molecules dissolved in 0.1 M KOH. The reduction peak at +0.23 V vs. RHE corresponds to the two-electron-two-proton reduction to form 5,10-dihydrophenazine. Figure 5b shows the CV curve of CB-conjugated benzene prepared by the reaction between oxidized CB and *o*-phenylenediamine. The potential of the reduction peak of the pyrazine moiety is +0.03 V vs. RHE, considerably more negative than that of phenazine molecules. This is ascribed to the fact that the pyrazine moiety is conjugated to the delocalized π system of the carbon support, and the additional reaction of this pyrazine moiety needs more energy. Figure 5c–e show the CV curves of the three CB-conjugated Co-complexes. The reduction and oxidation peaks of the pyrazine moieties in these complexes are at −0.08 V and −0.04 vs. RHE, respectively. The peaks of CB-conjugated Co-complexes are broader than that of CB-conjugated benzene, probably because the Co site modulates the electronic structure of the pyrazine moieties [30]. For CB-salophen-Co and CB-pda-Co, weak shoulder features can be observed at the anodic side of the main oxidation peaks. To figure out the origin of these features, the CV curves of CB-salophen and CB-pda were measured (Figures S5 and S6). Pyrazine moieties in these CB-conjugated ligands show a pair of redox peaks. In addition, the phenolic groups in CB-salophen and the diamine moieties in CB-pda also show redox features. However, when these CB-conjugated ligands form complexes with Co, these redox features should disappear. For CB-salophen, the oxidation peaks at −0.04 V and +0.07 V vs. RHE (Figure S5a) are assigned to the oxidation processes of pyrazine moieties (Figure S5c) and phenolic groups (Figure S5d), respectively. For CB-salophen-Co (Figure S5b), the area of the peak of phenolic groups is 21% of the area of the peak of pyrazine moieties, indicating that about 21% of the salophen ligands did not coordinate with Co in CB-salophen-Co. For CB-pda, the oxidation peaks at −0.04 V and + 0.03 V vs. RHE (Figure S6a) are assigned to the oxidation processes of pyrazine moieties (Figure S6c) and diamine moieties (Figure S6d), respectively. For CB-pda-Co (Figure S6b), the area of the peak of diamine moieties is 7% of the area of the peak of pyrazine moieties, indicating that about 7% of the pda ligands did not coordinate with Co in CB-pda-Co. Since the phenanthroline moieties in CB-phen are not involved in redox processes in the potential window of the CV curves, we cannot probe the percentage of the coordination between CB-phen and Co from the CV measurements. Nevertheless, the N:Co atomic ratio of CB-phen-Co is lower than that of CB-salophen-Co and CB-pda-Co (Table 1), indicating that the coordination reaction between Co and CB-phen was more complete. It is reliable to assume all ligands on CB-phen form complexes with Co, and the number of Co sites on CB-phen-Co equals the number of pyrazine moieties.
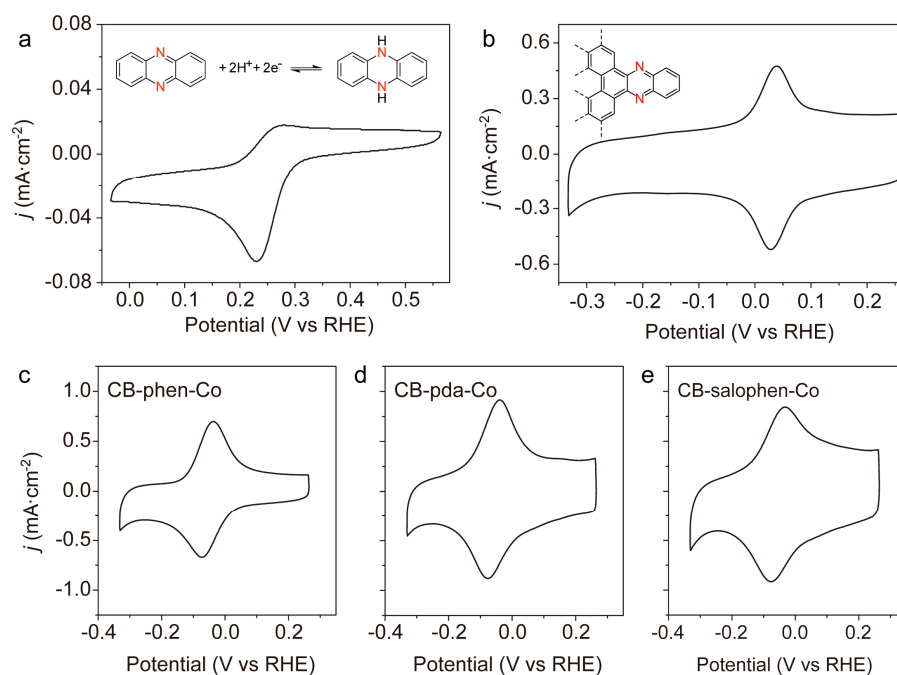
Figure 5. CV curves of (**a**) dissolved phenazine molecules, (**b**) CB-conjugated benzene, (**c**) CB-phen-Co, (**d**) CB-pda-Co and (**e**) CB-salophen-Co in Ar saturated solution of 0.1 M KOH. The sweeping rate is 10 mV·s^{-1}.

The density of the electrochemically active pyrazine moieties (n_{site}, unit: mol·cm^{-2}) was calculated from the area of the oxidation peak (A_{ox}, unit: A·cm^{-2}·V) according to:

$$n_{site} = \frac{A_{ox}}{2vF}$$

In this equation, v is the sweeping rate of the CV test (0.01 V·s^{-1}), and F is the Faradaic constant (96,485 C·mol^{-1}). For CB-conjugated complexes, each pyrazine moiety corresponds to one metal site. For CB-salophen-Co, the uncoordinated salophen ligands were excluded. Table 2 lists the total densities of Co sites from ICP-MS analysis and densities of the electrochemically active Co sites from the CV curves of the three CB-conjugated complexes (Figure 5c–e). Overall, 40% to 50% of the Co sites are electrochemically active for each sample.

Table 2. Comparison of the total density of Co sites from ICP-MS analysis and electrochemically active Co sites from CV curves (unit: nmol·cm^{-2}).

	Total Site Density	Electrochemically Active Site Density
CB-phen-Co	80.0	38.2
CB-pda-Co	88.7	40.9
CB-salophen-Co	84.9	36.0

It is noteworthy that the redox features of the Co sites are not shown in the CV curves in Figure 5. In general, the redox potential of Co^{3+}/Co^{2+} in Co-N-C single-atom catalysts was reported to be around 1 V vs. RHE [43,44]. It was also reported that during the ORR tests at the potential below 1 V vs. RHE, the Co sites were maintained at a +2 valence state [45]. Since the redox potentials of Co^{3+}/Co^{2+} and pyrazine moieties are well separated, the coordination between the conjugated ligands and Co showed little effect on the redox features of the pyrazine moieties shown in Figure 5. Figure S7 shows the CV curve of CB-phen-Co between 0.7 V and 1.3 V vs. RHE. Redox peaks of Co^{3+}/Co^{2+} around

1.1 V vs. RHE were observed. The area of the redox peaks decreased gradually during the CV measurement, indicating that the conjugated complexes were unstable at the high potential for this CV measurement.

The ORR performances of the three CB-conjugated complexes in the alkaline electrolyte of 0.1 M KOH were tested by RDE and RRDE. Figure S8 shows the results of RRDE tests. The four-electron reduction of O_2 to produce H_2O was the predominant reaction that occurred on all three catalysts, and the selectivity of H_2O_2 kept around 20% at the potential from 0.10 to 0.75 V vs. RHE (Figure S8d). Figure 6 shows the ORR polarization curves on RDE with different rotating speeds and the Koutecky-Levich plots of the CB-conjugated complexes. The limiting diffusion current densities of the three graphite-conjugated Co complexes were around 5.0–5.5 mA cm^{-2} at the rotating speed of 1600 rpm, in accordance with the reported Co-based single-atom catalysts [8,19,30]. The Koutecky-Levich plots were fitted according to the following equation [46]:

$$\frac{1}{j} = \frac{1}{j_k} + \frac{1}{j_d} = \frac{1}{j_k} + \frac{1}{0.62nFD_{O_2}^{2/3}\nu^{-1/6}C_{O_O}} \cdot \frac{1}{\omega^{-1/2}}$$
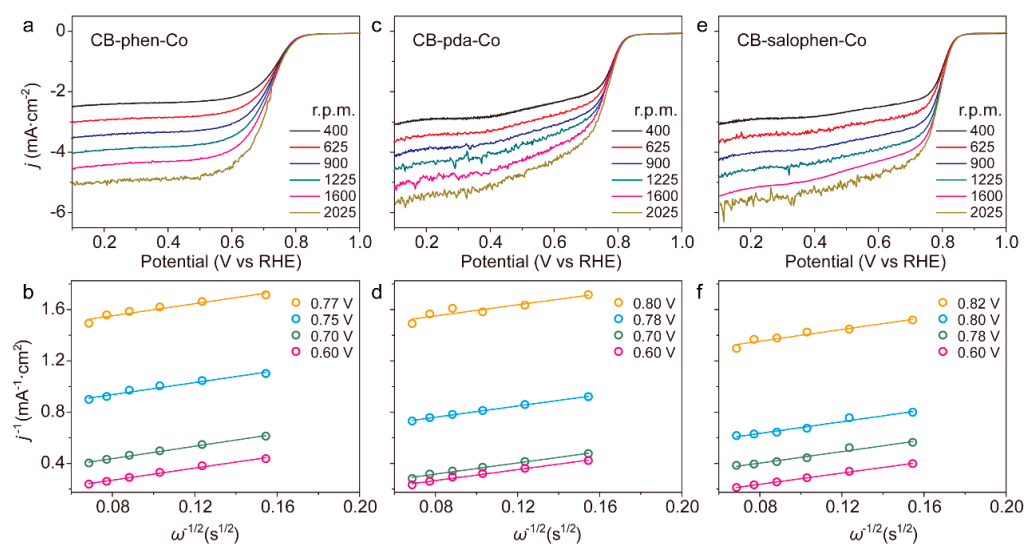

Figure 6. ORR performances of CB-conjugated complexes on RDE. Polarization curves (**a,c,e**) and Koutecky–Levich plots (**b,d,f**) of CB-phen-Co (**a,b**), CB-pda-Co (**c,d**) and CB-salophen-Co (**e,f**) in O_2 saturated electrolyte of 0.1 M KOH. The sweeping rate is 10 mV·s^{-1}.

In this equation, j is the ORR current density on RDE; j_k is the kinetics-controlled current density; j_d is the diffusion-controlled current density; n is the number of electrons transferred to one O_2 molecule; F is the Faradaic constant (96,485 C·mol^{-1}); D_{O2} is the diffusion coefficient of O_2 in water (1.93 × 10^{-5} cm^2·s^{-1}); ν is the kinematic viscosity of water (1.009 × 10^{-2} cm^2·s^{-1}); C_{O2} is the solubility of O_2 in water (1.26 × 10^{-3} mol·L^{-1}); and ω is the rotating speed of the RDE (unit: rad·s^{-1}) [47,48]. The numbers of electron transfer from the fitting results were 3.5, 3.6 and 3.6 at 0.60 V vs. RHE for CB-phen-Co, CB-pda-Co and CB-salophen-Co, respectively, close to the values from RRDE tests (Figure S8d). Then, j_k was calculated from j and the fitted numbers of n. Finally, the intrinsic TOF of one Co site can be calculated from j_k and the density of electrochemical active Co sites (n_{site}) according to:

$$\text{TOF} = \frac{j_k}{nFn_{site}}$$

Figure 7a compares the TOFs of the three CB-conjugated complexes. At the potential between 0.7 and 0.9 V vs. RHE, CB-salophen-Co showed the highest TOF, and CB-phen-Co showed the lowest TOF. At 0.80 V vs. RHE, the TOF of CB-salophen-Co was 0.19 s^{-1}, equaled 3.9 times that of the TOF of CB-pda-Co and 8.4 times that of the TOF of CB-

phen-Co. At 0.75 V vs. RHE, the TOF of CB-salophen-Co reached 0.72 s^{-1}, equaled 2.7 times that of the TOF of CB-pda-Co and 6.6 times that of the TOF of CB-phen-Co (Figure 7b). These results imply that the CoN$_2$O$_2$ local structure possesses superior intrinsic activity towards ORR. It was reported that the anionic oxygen ligands in the CoN$_2$O$_2$ local structure push the π-back donation from Co to the nitrogen ligands [49]. This effect can lead to lower occupancy of the 3d orbitals of Co and a stronger binding of oxygen-containing species (O, OH and OOH) [50]. Since the binding strength of oxygen-containing species on most Co-based single-atom sites is weaker than the optimized strength to facilitate the kinetics of 4-electron ORR [51,52], the increase in binding strength induced by the oxygen ligands in CoN$_2$O$_2$ local structure is the probable reason for the high TOF of CB-salophen-Co. Figure 7c shows the Tafel plots of the CB-conjugated complexes. The Tafel slopes of these catalysts were different, indicating different rate-determining steps on each catalyst. The mechanism of ORR under alkaline conditions is proposed as follows [52,53]:
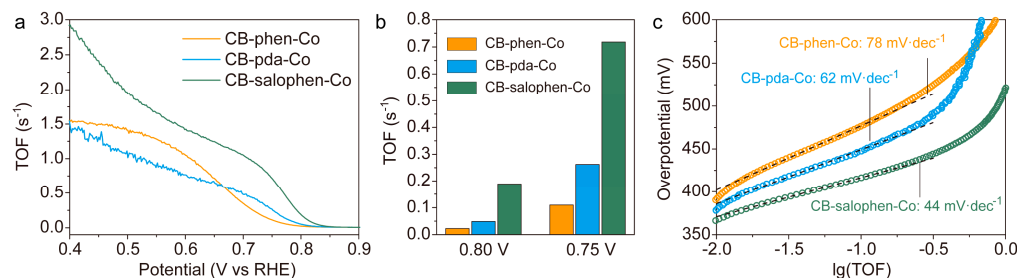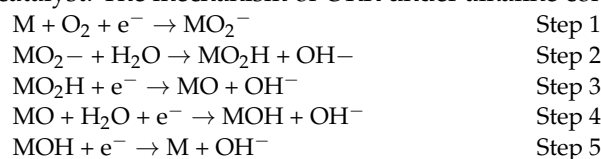
$$M + O_2 + e^- \rightarrow MO_2^- \qquad \text{Step 1}$$
$$MO_2^- + H_2O \rightarrow MO_2H + OH- \qquad \text{Step 2}$$
$$MO_2H + e^- \rightarrow MO + OH^- \qquad \text{Step 3}$$
$$MO + H_2O + e^- \rightarrow MOH + OH^- \qquad \text{Step 4}$$
$$MOH + e^- \rightarrow M + OH^- \qquad \text{Step 5}$$

Figure 7. Comparison of ORR activity of CB-conjugated complexes. (**a**) Curves of TOF based on the potential. (**b**) Comparison of TOF at 0.80 V and 0.75 V vs. RHE. (**c**) Tafel plots. The Tafel slope of each catalyst is indicated.

In the above steps, M represents the catalytic site. The Tafel slope close to 118 mV·dec^{-1} indicates that the rate is determined by the initial electron transfer step (Step **1**). The Tafel slope close to 59 mV·dec^{-1} indicates that the rate-determining step is the protonation of the MO$_2^-$ species (Step **2**) after the first electron transfer step. The Tafel slope close to 40 mV·dec^{-1} indicates the second electron transfer step (Step **3**) to be the rate-determining step [54]. As indicated by Figure 7c, the rate-determining steps of ORR on CB-pda-Co and CB-salophen-Co should be Step **2** and Step **3**, respectively. The Tafel slope of ORR on CB-phen-Co (78 mV·dec^{-1}) is between 59 and 118 mV·dec^{-1}, implying the rate was not limited solely by one step. The Tafel slopes of all catalysts increased at the high overpotential side, probably due to the substantial increase in the coverage of MO$_2$H species at high overpotential.

3. Materials and Methods

3.1. Preparation of Carbon-Conjugated Co Complexes

Scheme 1 shows the strategy for the preparation of carbon-conjugated Co complexes. First, carbon black support (**1**) was oxidized to generate *o*-quinone moieties at the edge of the carbon layer (**2**). Ligands were then conjugated to the carbon support through the condensation of *o*-phenylenediamines moieties on the ligands with *o*-quinone moieties on the support. Finally, Co(II) salts were added to form complexes with the conjugated ligands. We used PAQ as the analog of *o*-quinone moieties in oxidized CB to estimate the conversion yield of each reaction step. The schematic diagram of model reactions and their conversion yields are shown in Scheme S1. PAQ and other reactants were added according to their stoichiometric ratios. However, in the preparation of CB-conjugated complexes,

the small-molecule reactants (**3**, **6**, **9** and $CoCl_2$) were added in great excess relative to the *o*-quinone moieties in the oxidized CB. Therefore, the actual conversion yield based on the quantity of active sites on CB should be substantially higher than the values in Scheme S1.

3.1.1. Oxidation of Carbon Black

First, the H_2SO_4 solution with a mass fraction of 60% was obtained by slowly diluting 21.4 mL of 98% sulfuric acid in 13.6 mL of distilled water under an ice bath. Then, 500 mg of Ketjen black (EC-300J, Guangdong Canrd New Energy Technology Co., Ltd., Dongguan, China) was dispersed into the H_2SO_4 solution, after which 2 g of sodium bromate ($NaBrO_3$) was slowly added into the reaction vessel within 10 min with continuous magnetic stirring. The vessel was sealed and kept at room temperature for 24 h. The resulting oxidized carbon black was collected by filtration, rinsed with pure water and ethanol, and finally placed in an oven at 100 °C overnight.

3.1.2. Synthesis of CB-pda

Then, 160 mg of oxidized CB was dispersed in 40 mL of ethanol (extra dry) containing 90.8 mg of 1,2,4,5-tetraaminobenzene tetrahydrochloride and 512 mg of $KHCO_3$. Afterward, the reaction vessel was purged with Ar, sealed, and heated at 60 °C for 12 h. After naturally cooling to room temperature, the solid was collected by centrifugation and washed with ethanol. The product was then immersed in 0.1 M $HClO_4$ for 1 h and 0.1 M KOH for 10 min in sequence. CB-pda was obtained by collecting the resulting powder, washing it with deionized water and ethanol, and drying it at 60 °C in a vacuum oven.

3.1.3. Synthesis of CB-salophen

Then, 80 mg of CB-pda was firstly dispersed in 20 mL of dry ethanol in a flask, then 200 μL of salicylaldehyde was added via a pipette with magnetic stirring. After that, the flask was coupled with a reflux condenser and held at 80 °C for 8 h under an Ar atmosphere. Upon cooling, the resulting product was separated by centrifugation, washed thoroughly with ethanol, and dried under a vacuum.

3.1.4. Synthesis of CB-phen

Then, 120 mg of oxidized CB was uniformly dispersed in 40 mL of dry ethanol, dissolving 50 mg of 5,6-diamino-1,10-phenanthroline. The reaction suspension was subsequently stirred at 60 °C for 10 h with the protection of Ar. After the reaction vessel was cooled down to ambient temperature, the functionalized carbon was collected and rinsed with ethanol three times. Next, the as-obtained powder was dispersed in 0.1 M $HClO_4$ solution for 1 h. After rinsing with deionized water and ethanol, the sample was dried in a vacuum oven.

3.1.5. Synthesis of CB-pda-Co, CB-salophen-Co and CB-phen-Co

For the synthesis of CB-pda-Co, 50 mg of CB-pda and 50 mg of cobalt chloride were added into a flask charged with a stir bar. Subsequently, the flask was pumped, refilled with Ar, and sealed with a rubber stopper. Then, 10 mL of dry ethanol was then injected via a syringe. After being continuously stirred at ambient temperature with the protection of Ar gas for 24 h, the CB-pda-Co was collected by centrifugation (Hunan Herexi Instrument & Equipment Co., Ltd., Changsha, China) with a rotating speed of 10,000 rpm for 5 minutes, rinsed with ethanol thoroughly, and dried in a vacuo. CB-salophen-Co and CB-phen-Co were prepared with a similar synthetic method, where CB-pda was replaced by 50 mg of CB-salophen or CB-phen, respectively.

3.2. *Characterizations*

X-ray photoelectron spectroscopy (XPS) analysis was carried out on a ULVAC-PHI 5000 VersaProbe III XPS system (ULVAC-PHI, Inc., Chigasaki, Japan), using a monochromatic Al Kα radiation (1486.6 eV). Powder X-ray diffraction (XRD) patterns were collected on a

Rigaku SmartLab X-ray powder diffractometer with Cu Kα radiation (Rigaku Corporation, Tokyo, Japan). Inductively coupled plasma mass spectrometry (ICP-MS) was performed using an Agilent 7700X instrument (Agilent Technologies, Inc., Santa Clara, CA, USA). High-angle annular dark-field scanning transmission electron microscopy (HAADF-STEM) images were collected on an FEI Titan Themis G2 at 300 kV with spherical aberration correction (Thermo Fisher Scientific Inc., Waltham, MA, USA).

3.3. Electrochemical Measurements

The electrochemical experiments for all of the samples were performed using a CHI 760E electrochemical workstation (CH Instruments, Inc., Shanghai, China). A standard three-electrode system was employed, where a Pt wire and a Hg/HgO electrode were used as the counter electrode and reference electrode, respectively. A rotating disk electrode (RDE) or rotating ring-disk electrode (RRDE) served as the working electrode. The catalyst inks were prepared by adding 4 mg of catalyst into 980 μL of ethanol and ultrasound for 30 min, followed by the addition of 20 μL of 5 wt% Nafion solution and further ultrasonication for another 3 h. Then, 10 μL or 6 μL of catalyst ink was uniformly loaded onto RDE or RRDE, followed by drying under an infrared lamp. All of the measured potentials were converted to the reversible hydrogen electrode (RHE) scale as follows, $E_{RHE} = E_{Hg/HgO} + 0.098 + 0.059$ pH. Prior to the electrochemical tests, the electrolyte was bubbled with Ar or O_2 flow for at least 30 min to achieve an Ar/O_2 saturated electrolyte. The CV curves of the samples were recorded in Ar-saturated 0.1 M KOH at a scan rate of 10 mV·s^{-1}. The area of the oxidation peak in the CV curves was measured by integrating the oxidation current density from -0.2 V to $+0.2$ V vs. RHE, with a straight line from the starting point to the ending point as the baseline, as illustrated in Figure S5a,b. Linear sweep voltammetry (LSV) was conducted in O_2-saturated 0.1 M KOH at a scan rate of 10 mV·s^{-1} with rotating speeds ranging from 400 to 2025 rpm.

The hydrogen peroxide (H_2O_2) selectivity and electron transfer number (*n*) of ORR were determined using the following equations:

$$H_2O_2 \text{ selectivity } (\%) = 200 \times \frac{I_r/N}{I_r/N + I_d}$$

$$n = 4 \times \frac{I_d}{I_r/N + I_d}$$

where I_r and I_d are the ring and disk current, and N is the current collection efficiency, which is 0.424 for the RRDE used here.

4. Conclusions

CB-conjugated Co complexes were prepared through the condensation reaction between *o*-quinone moieties on CB and *o*-phenylenediamine moieties on the ligands of the complexes. These complexes served as model heterogeneous catalysts with well-defined coordination structures of the Co-sites. The number of electrochemically accessible Co sites can be examined from the area of the redox peaks of the pyrazine linker between CB and the conjugated complexes in the CV curves. Thus, TOFs of the Co sites can be calculated. The ORR activity of the CB-conjugated Co complexes was measured in the alkaline condition. The TOF of ORR increased in the order of CB-phen-Co < CB-pda-Co < CB-salophen-Co. This work provides an effective strategy to unveil the structure–property relationship between the intrinsic electrocatalytic activity and the coordination structure of the metal sites. This strategy can be further used to explore and verify the possible local structure of the active sites proposed for the popular TM-N-C single-atom catalysts. DFT and ab initio molecular dynamics (MD) simulations can be conducted based on the well-defined local structure of CB-conjugated complexes to develop the theory of how the local structures of the TM sites affect the intrinsic electrocatalytic activity.

References

1. Wang, A.; Li, J.; Zhang, T. Heterogeneous single-atom catalysis. *Nat. Rev. Chem.* **2018**, *2*, 65–81. [CrossRef]
2. Kaiser, S.K.; Chen, Z.; Faust Akl, D.; Mitchell, S.; Perez-Ramirez, J. Single-Atom Catalysts across the Periodic Table. *Chem. Rev.* **2020**, *120*, 11703–11809. [CrossRef] [PubMed]
3. Yang, Y.; Yang, Y.; Pei, Z.; Wu, K.-H.; Tan, C.; Wang, H.; Wei, L.; Mahmood, A.; Yan, C.; Dong, J.; et al. Recent Progress of Carbon-Supported Single-Atom Catalysts for Energy Conversion and Storage. *Matter* **2020**, *3*, 1442–1476. [CrossRef]
4. Gu, J.; Hsu, C.S.; Bai, L.; Chen, H.M.; Hu, X. Atomically dispersed Fe^{3+} sites catalyze efficient CO_2 electroreduction to CO. *Science* **2019**, *364*, 1091–1094. [CrossRef]
5. Jin, Z.; Li, P.; Meng, Y.; Fang, Z.; Xiao, D.; Yu, G. Understanding the inter-site distance effect in single-atom catalysts for oxygen electroreduction. *Nat. Catal.* **2021**, *4*, 615–622. [CrossRef]
6. Chen, Y.; Ji, S.; Chen, C.; Peng, Q.; Wang, D.; Li, Y. Single-Atom Catalysts: Synthetic Strategies and Electrochemical Applications. *Joule* **2018**, *2*, 1242–1264. [CrossRef]
7. Sun, T.; Li, Y.; Cui, T.; Xu, L.; Wang, Y.G.; Chen, W.; Zhang, P.; Zheng, T.; Fu, X.; Zhang, S.; et al. Engineering of Coordination Environment and Multiscale Structure in Single-Site Copper Catalyst for Superior Electrocatalytic Oxygen Reduction. *Nano Lett.* **2020**, *20*, 6206–6214. [CrossRef] [PubMed]
8. Yuan, S.; Zhang, J.; Hu, L.; Li, J.; Li, S.; Gao, Y.; Zhang, Q.; Gu, L.; Yang, W.; Feng, X.; et al. Decarboxylation-Induced Defects in MOF-Derived Single Cobalt Atom@Carbon Electrocatalysts for Efficient Oxygen Reduction. *Angew. Chem. Int. Ed.* **2021**, *60*, 21685–21690. [CrossRef]
9. Li, F.; Han, G.-F.; Noh, H.-J.; Kim, S.-J.; Lu, Y.; Jeong, H.Y.; Fu, Z.; Baek, J.-B. Boosting oxygen reduction catalysis with abundant copper single atom active sites. *Energy Environ. Sci.* **2018**, *11*, 2263–2269. [CrossRef]
10. Zhang, X.; Xu, X.; Yao, S.; Hao, C.; Pan, C.; Xiang, X.; Tian, Z.Q.; Shen, P.K.; Shao, Z.; Jiang, S.P. Boosting Electrocatalytic Activity of Single Atom Catalysts Supported on Nitrogen-Doped Carbon through N Coordination Environment Engineering. *Small* **2022**, *18*, e2105329. [CrossRef]
11. Liu, S.; Li, C.; Zachman, M.J.; Zeng, Y.; Yu, H.; Li, B.; Wang, M.; Braaten, J.; Liu, J.; Meyer, H.M.; et al. Atomically dispersed iron sites with a nitrogen–carbon coating as highly active and durable oxygen reduction catalysts for fuel cells. *Nat. Energy* **2022**, *7*, 652–663. [CrossRef]
12. Yin, P.; Yao, T.; Wu, Y.; Zheng, L.; Lin, Y.; Liu, W.; Ju, H.; Zhu, J.; Hong, X.; Deng, Z.; et al. Single Cobalt Atoms with Precise N-Coordination as Superior Oxygen Reduction Reaction Catalysts. *Angew. Chem. Int. Ed.* **2016**, *55*, 10800–10805. [CrossRef] [PubMed]

13. Yang, J.; Liu, W.; Xu, M.; Liu, X.; Qi, H.; Zhang, L.; Yang, X.; Niu, S.; Zhou, D.; Liu, Y.; et al. Dynamic Behavior of Single-Atom Catalysts in Electrocatalysis: Identification of Cu-N$_3$ as an Active Site for the Oxygen Reduction Reaction. *J. Am. Chem. Soc.* **2021**, *143*, 14530–14539. [CrossRef] [PubMed]

14. Gao, Y.; Cai, Z.; Wu, X.; Lv, Z.; Wu, P.; Cai, C. Graphdiyne-Supported Single-Atom-Sized Fe Catalysts for the Oxygen Reduction Reaction: DFT Predictions and Experimental Validations. *ACS Catal.* **2018**, *8*, 10364–10374. [CrossRef]

15. Zhang, J.; Zhao, Y.; Chen, C.; Huang, Y.C.; Dong, C.L.; Chen, C.J.; Liu, R.S.; Wang, C.; Yan, K.; Li, Y.; et al. Tuning the Coordination Environment in Single-Atom Catalysts to Achieve Highly Efficient Oxygen Reduction Reactions. *J. Am. Chem. Soc.* **2019**, *141*, 20118–20126. [CrossRef]

16. Li, J.; Li, H.; Xie, W.; Li, S.; Song, Y.; Fan, K.; Lee, J.Y.; Shao, M. Flame-Assisted Synthesis of O-Coordinated Single-Atom Catalysts for Efficient Electrocatalytic Oxygen Reduction and Hydrogen Evolution Reaction. *Small Methods* **2022**, *6*, e2101324. [CrossRef]

17. Cheng, Y.; Zhao, S.; Li, H.; He, S.; Veder, J.-P.; Johannessen, B.; Xiao, J.; Lu, S.; Pan, J.; Chisholm, M.F.; et al. Unsaturated edge-anchored Ni single atoms on porous microwave exfoliated graphene oxide for electrochemical CO$_2$. *Appl. Catal. B* **2019**, *243*, 294–303. [CrossRef]

18. Xu, W.; Sun, Y.; Zhou, J.; Cao, M.; Luo, J.; Mao, H.; Hu, P.; Gu, H.; Zhai, H.; Shang, H.; et al. Coordinatively unsaturated single Co atoms immobilized on C$_2$N for efficient oxygen reduction reaction. *Nano Res.* **2022**. [CrossRef]

19. Shen, H.; Gracia-Espino, E.; Ma, J.; Tang, H.; Mamat, X.; Wagberg, T.; Hu, G.; Guo, S. Atomically FeN$_2$ moieties dispersed on mesoporous carbon: A new atomic catalyst for efficient oxygen reduction catalysis. *Nano Energy* **2017**, *35*, 9–16. [CrossRef]

20. Xia, B.Y.; Yan, Y.; Li, N.; Wu, H.B.; Lou, X.W.; Wang, X. A metal–organic framework-derived bifunctional oxygen electrocatalyst. *Nat. Energy* **2016**, *1*. [CrossRef]

21. Zhang, Z.; Sun, J.; Wang, F.; Dai, L. Efficient Oxygen Reduction Reaction (ORR) Catalysts Based on Single Iron Atoms Dispersed on a Hierarchically Structured Porous Carbon Framework. *Angew. Chem. Int. Ed.* **2018**, *57*, 9038–9043. [CrossRef]

22. Christopher, P. Single-Atom Catalysts: Are All Sites Created Equal? *ACS Energy Lett.* **2019**, *4*, 2249–2250. [CrossRef]

23. Zhu, C.; Fu, S.; Shi, Q.; Du, D.; Lin, Y. Single-Atom Electrocatalysts. *Angew. Chem. Int. Ed.* **2017**, *56*, 13944–13960. [CrossRef] [PubMed]

24. Sun, Z.; Liu, Q.; Yao, T.; Yan, W.; Wei, S. X-ray absorption fine structure spectroscopy in nanomaterials. *Sci. China Mater.* **2015**, *58*, 313–341. [CrossRef]

25. Li, X.; Cao, C.-S.; Hung, S.-F.; Lu, Y.-R.; Cai, W.; Rykov, A.I.; Miao, S.; Xi, S.; Yang, H.; Hu, Z.; et al. Identification of the Electronic and Structural Dynamics of Catalytic Centers in Single-Fe-Atom Material. *Chemistry* **2020**, *6*, 3440–3454. [CrossRef]

26. Fei, H.; Dong, J.; Feng, Y.; Allen, C.S.; Wan, C.; Volosskiy, B.; Li, M.; Zhao, Z.; Wang, Y.; Sun, H.; et al. General synthesis and definitive structural identification of MN$_4$C$_4$ single-atom catalysts with tunable electrocatalytic activities. *Nat. Catal.* **2018**, *1*, 63–72. [CrossRef]

27. Fukushima, T.; Drisdell, W.; Yano, J.; Surendranath, Y. Graphite-Conjugated Pyrazines as Molecularly Tunable Heterogeneous Electrocatalysts. *J. Am. Chem. Soc.* **2015**, *137*, 10926–10929. [CrossRef] [PubMed]

28. Jackson, M.N.; Oh, S.; Kaminsky, C.J.; Chu, S.B.; Zhang, G.; Miller, J.T.; Surendranath, Y. Strong Electronic Coupling of Molecular Sites to Graphitic Electrodes via Pyrazine Conjugation. *J. Am. Chem. Soc.* **2018**, *140*, 1004–1010. [CrossRef]

29. Jackson, M.N.; Surendranath, Y. Molecular Control of Heterogeneous Electrocatalysis through Graphite Conjugation. *Acc. Chem. Res.* **2019**, *52*, 3432–3441. [CrossRef]

30. Kaminsky, C.J.; Wright, J.; Surendranath, Y. Graphite-Conjugation Enhances Porphyrin Electrocatalysis. *ACS Catal.* **2019**, *9*, 3667–3671. [CrossRef]

31. Jackson, M.N.; Pegis, M.L.; Surendranath, Y. Graphite-Conjugated Acids Reveal a Molecular Framework for Proton-Coupled Electron Transfer at Electrode Surfaces. *ACS Cent. Sci.* **2019**, *5*, 831–841. [CrossRef] [PubMed]

32. Jackson, M.N.; Kaminsky, C.J.; Oh, S.; Melville, J.F.; Surendranath, Y. Graphite Conjugation Eliminates Redox Intermediates in Molecular Electrocatalysis. *J. Am. Chem. Soc.* **2019**, *141*, 14160–14167. [CrossRef] [PubMed]

33. Braley, S.E.; Xie, J.; Losovyj, Y.; Smith, J.M. Graphite Conjugation of a Macrocyclic Cobalt Complex Enhances Nitrite Electroreduction to Ammonia. *J. Am. Chem. Soc.* **2021**, *143*, 7203–7208. [CrossRef]

34. Toshiaki, O.; Masamichi, Y.; Haruo, K. X-Ray Photoelectron Spectroscopy of *p*-Benzoquinone, Hydroquinone and Their Halogen-Substituted Derivatives. *Bull. Chem. Soc. Jpn.* **1974**, *47*, 1158–1161. [CrossRef]

35. Chastain, J.; King, R.C. *Handbook of X-ray Photoelectron Spectroscopy*; Perkin-Elmer Corporation, Physical Electronics Division: Eden Prairie, MN, USA, 1992.

36. Ferragina, C.; Massucci, M.A.; Mattogno, G. XPS studies on the host-guest interaction of 2,2′-Bipyridyl, 1,10-phenanthroline and 2,9-dimethyl-1,10-phenanthroline intercalated in α-zirconium phosphate. *J. Inclusion Phenom. Mol. Recognit. Chem.* **1989**, *7*, 529–536. [CrossRef]

37. Mattogno, G.; Ferragina, C.; Massucci, M.A.; Patrono, P.; La Ginestra, A. X-ray photoelectron spectroscopic evidence of interlayer complex formation between Co(II) and N-heterocycles in α-Zr(hpo$_4$)$_2$ · H$_2$O. *J. Electron Spectrosc. Relat. Phenom.* **1988**, *46*, 285–295. [CrossRef]

38. Ju, W.; Bagger, A.; Hao, G.-P.; Varela, A.S.; Sinev, I.; Bon, V.; Roldan Cuenya, B.; Kaskel, S.; Rossmeisl, J.; Strasser, P. Understanding activity and selectivity of metal-nitrogen-doped carbon catalysts for electrochemical reduction of CO$_2$. *Nat. Commun.* **2017**, *8*, 944. [CrossRef]

39. Xu, X.; Friend, C.M. The adsorption and reactions of aniline on Rh(111). *J. Vac. Sci. Technol. A* **1991**, *9*, 1599–1603. [CrossRef]

40. Srinivasan, V.; Walton, R.A. X-ray photoelectron spectra of inorganic molecules. XX. Observations concerning the sulfur 2p binding energies in metal complexes of thiourea. *Inorg. Chim. Acta* **1977**, *25*, L85–L86. [CrossRef]

41. Dash, K.C.; Folkesson, B.; Larsson, R.; Mohapatra, M. An XPS investigation on a series of schiff base dioxime ligands and cobalt complexes. *J. Electron Spectrosc. Relat. Phenom.* **1989**, *49*, 343–357. [CrossRef]

42. Hisashi, O.; Sigeo, K. Binuclear metal complexes. III. Preparation and properties of mononuclear and binuclear copper(II) and nickel(II) complexes of new macrocycles and their related ligands. *B. Chem. Soc. Jpn.* **1972**, *45*, 1759–1764. [CrossRef]

43. Park, H.; Oh, S.; Lee, S.; Choi, S.; Oh, M. Cobalt- and nitrogen-codoped porous carbon catalyst made from core–shell type hybrid metal–organic framework (ZIF-L@ZIF-67) and its efficient oxygen reduction reaction (ORR) activity. *Appl. Catal. B-Environ.* **2019**, *246*, 322–329. [CrossRef]

44. Lian, Y.; Yang, W.; Zhang, C.; Sun, H.; Deng, Z.; Xu, W.; Song, L.; Ouyang, Z.; Wang, Z.; Guo, J.; et al. Unpaired 3d electrons on atomically dispersed cobalt centres in coordination polymers regulate both oxygen reduction reaction (ORR) activity and selectivity for use in zinc-air batteries. *Angew. Chem. Int. Ed.* **2020**, *59*, 286–294. [CrossRef]

45. Zitolo, A.; Ranjbar-Sahraie, N.; Mineva, T.; Li, J.; Jia, Q.; Stamatin, S.; Harrington, G.F.; Lyth, S.M.; Krtil, P.; Mukerjee, S.; et al. Identification of catalytic sites in cobalt-nitrogen-carbon materials for the oxygen reduction reaction. *Nat. Commun.* **2017**, *8*, 957. [CrossRef] [PubMed]

46. Bard, A.J.; Faulkner, L.R. *Electrochemical methods: Fundamentals and applications*, 2nd. ed.; John Wiley & Sons, Inc.: New York, NY, USA, 2001.

47. Zhang, J.; Mo, Y.; Vukmirovic, M.B.; Klie, R.; Sasaki, K.; Adzic, R.R. Platinum Monolayer Electrocatalysts for O_2 Reduction: Pt Monolayer on Pd(111) and on Carbon-Supported Pd Nanoparticles. *J. Phys. Chem. B* **2004**, *108*, 10955–10964. [CrossRef]

48. Gu, J.; Lan, G.; Jiang, Y.; Xu, Y.; Zhu, W.; Jin, C.; Zhang, Y. Shaped Pt-Ni nanocrystals with an ultrathin Pt-enriched shell derived from one-pot hydrothermal synthesis as active electrocatalysts for oxygen reduction. *Nano Res.* **2015**, *8*, 1480–1496. [CrossRef]

49. Nichols, A.W.; Cook, E.N.; Gan, Y.J.; Miedaner, P.R.; Dressel, J.M.; Dickie, D.A.; Shafaat, H.S.; Machan, C.W. Pendent relay enhances H_2O_2 selectivity during dioxygen reduction mediated by bipyridine-based $Co-N_2O_2$ Complexes. *J. Am. Chem. Soc.* **2021**, *143*, 13065–13073. [CrossRef]

50. Nilsson, A.; Pettersson, L.G.M.; Hammer, B.; Bligaard, T.; Christensen, C.H.; Nørskov, J.K. The electronic structure effect in heterogeneous catalysis. *Catal. Lett.* **2005**, *100*, 111–114. [CrossRef]

51. Zagal, J.H.; Koper, M.T.M. Reactivity descriptors for the activity of molecular MN_4 catalysts for the oxygen reduction reaction. *Angew. Chem. Int. Ed.* **2016**, *55*, 14510–14521. [CrossRef]

52. Zhong, L.; Li, S. Unconventional oxygen reduction reaction mechanism and scaling relation on single-atom catalysts. *ACS Catal.* **2020**, *10*, 4313–4318. [CrossRef]

53. Shinagawa, T.; Garcia-Esparza, A.T.; Takanabe, K. Insight on Tafel slopes from a microkinetic analysis of aqueous electrocatalysis for energy conversion. *Sci. Rep.* **2015**, *5*, 13801. [CrossRef] [PubMed]

54. Liu, J.; Cheng, T.; Jiang, L.; Zhang, H.; Shan, Y.; Kong, A. Efficient nitrate and oxygen electroreduction over pyrolysis-free mesoporous covalent Co-salophen coordination frameworks on carbon nanotubes. *Electrochim. Acta* **2020**, *363*, 137280. [CrossRef]